

## Article

# Corrosion Protection Oxide Scale Formed on Surface of Fe-Ni-M (M = Al, Cr, Cu) Inert Anode for Molten Salt Electrolysis

Myungjae Kim <sup>1</sup>, Jungshin Kang <sup>2,3</sup>, Jiwoo Kim <sup>1</sup> and Jiwoong Kim <sup>1,\*</sup>

<sup>1</sup> Department of Organic Materials and Fiber Engineering, Soongsil University, Seoul 06978, Korea; kmj9733@gmail.com (M.K.); jiwook725@gmail.com (J.K.)

<sup>2</sup> Korea Institute of Geoscience and Mineral Resources, Daejeon 34132, Korea; jskang@kigam.re.kr

<sup>3</sup> Department of Resources Recycling, University of Science and Technology, Daejeon 34133, Korea

\* Correspondence: jwk@ssu.ac.kr; Tel.: +82-2-828-7046

**Abstract:** An oxide scale formed on the surface of metal anodes is crucial for determining the overall quality of molten salt electrolysis (MSE), particularly for the durability of the anode materials. However, the material properties of oxide scales are yet to be revealed, particularly in ternary spinel oxide phases. Therefore, we investigate the mechanical and thermal properties of spinel oxides via first-principles calculations. The oxides are calculated using the models of normal (cubic) and inverse (orthorhombic) spinel compounds. The d-orbital exchange correlation potential of transition metal oxides is addressed using the generalized gradient approximation plus Hubbard U. The lattice constant, formation energy, cohesive energy, elastic modulus, Poisson's ratio, universal anisotropy index, hardness, minimal thermal conductivity, and thermal expansion coefficient are calculated. Based on the calculated mechanical and thermal properties of the spinel compound, the Fe-Ni-Al inert anode is expected to be the most suitable oxide scale for MSE applications among the materials investigated in our study.

**Keywords:** first-principles calculation; inert anode; spinel compound; elastic property; thermal property



**Citation:** Kim, M.; Kang, J.; Kim, J.; Kim, J. Corrosion Protection Oxide Scale Formed on Surface of Fe-Ni-M (M = Al, Cr, Cu) Inert Anode for Molten Salt Electrolysis. *Materials* **2022**, *15*, 719. <https://doi.org/10.3390/ma15030719>

Academic Editor: Fuhui Wang

Received: 3 December 2021

Accepted: 17 January 2022

Published: 18 January 2022

**Publisher's Note:** MDPI stays neutral with regard to jurisdictional claims in published maps and institutional affiliations.



**Copyright:** © 2022 by the authors. Licensee MDPI, Basel, Switzerland. This article is an open access article distributed under the terms and conditions of the Creative Commons Attribution (CC BY) license (<https://creativecommons.org/licenses/by/4.0/>).

## 1. Introduction

The carbon anodes used in the primary metal (Mg, Al, and Ti) industry inevitably result in high energy consumption, severe air pollution, and other problems [1,2]. Therefore, inert anodes are in high demand as they reduce the production of greenhouse and other harmful gases such as CO<sub>2</sub>, C<sub>2</sub>F<sub>6</sub>, and CF<sub>4</sub> [3–6]. In addition, although the molten salt electrolysis (MSE) method is advantageous, it requires the use of expensive noble metal (Ag, Pt, Pd, and Ir) anodes [7–9].

Among inert anode materials, Fe-Ni-based alloy anodes are good candidates because of their excellent mechanical properties, electrical conductivity, cracking resistance, good thermal shock resistance, and ease of fabrication [10,11]. In the initial stage of electrolysis, several types of oxides are formed as scales on the surface of the anode. These oxide scales protect the alloy anode against highly corrosive conditions [12,13]. However, certain problems occur such as poor contact with molten salt, poor adhesion of the oxide scale, heterogeneous oxide scale growth, and formation of a thick oxide scale.

Therefore, studies regarding ternary inert anodes with other elements added to Fe-Ni based anodes are actively being conducted. In particular, Fe-Ni-Cr, Fe-Ni-Cu, and Fe-Ni-Al inert anodes are garnering considerable attention. In general, the corrosion of the anode surface yields oxide scales composed of binary oxides (Fe<sub>2</sub>O<sub>3</sub>, Fe<sub>3</sub>O<sub>4</sub>, NiO, Cr<sub>2</sub>O<sub>3</sub>, and Al<sub>2</sub>O<sub>3</sub>) and spinel compounds (NiFe<sub>2</sub>O<sub>4</sub>, FeAl<sub>2</sub>O<sub>4</sub>, CrFe<sub>2</sub>O<sub>4</sub>, and CuFe<sub>2</sub>O<sub>4</sub>) [14,15]. Although binary oxide scales have been extensively investigated, information regarding the thermal and mechanical properties of spinel compounds remains insufficient. Hence, in this study, we investigated spinel oxide scales, to which Al, Cr, and Cu were added.

For a normal spinel compound, the face-centered cubic (fcc) sites of the tetrahedron are occupied by  $1/8$  of  $A^{2+}$ , and on the other side,  $16/32$  of the octahedral sites are occupied by  $B^{3+}$ . Conversely, the inverted spinel compound occupies half of the octahedral sites,  $B^{3+}$  and  $A^{2+}$ , and the other half of  $B^{3+}$  occupies tetrahedral sites [16]. The two structures can be written in the form  $A_X(B_2)_Y O_4$  and  $B_X(AB)_Y O_4$ , where  $X$  and  $Y$  represent the tetrahedral and octahedral sites of the normal and inverse spinel compounds, respectively [17]. In general, the metal ion preference for octahedral site occupation is  $Cu^{2+} > Cr^{2+} > Ni^{2+} > Mn^{3+} > Al^{3+} > Fe^{2+} > Co^{2+} > Fe^{3+} > Mn^{2+}$  [18]. This sequence shows that  $FeNi_2O_4$ ,  $FeCr_2O_4$ , and  $FeCu_2O_4$  are the inverse spinel phases with the molecular formula  $B^{3+}(A^{2+}B^{3+})O_4$ . Therefore,  $AlFe_2O_4$  is an inverse spinel phase with the molecular formula  $Fe^{3+}(Fe^{2+}Al^{3+})O_4$ . All  $Al^{3+}$  cations occupy the octahedral sites, and Fe cations are distributed similarly between the octahedral and tetrahedral sites. Conversely,  $FeAl_2O_4$  is a normal spinel-type structure. Based on the content of the cation ( $Al^{3+}$ , and  $Fe^{3+}$ ) in tetrahedral sites,  $FeAl_2O_4$  and  $AlFe_2O_4$  are classified as normal and inverse spinel compounds, respectively [19].

The purpose of this study is to investigate the thermal and mechanical properties of normal and inverse spinel compounds that inevitably form on an alloy-based inert anode. First-principles calculations were performed to analyze the structural properties of  $n\text{-NiFe}_2O_4$ ,  $n\text{-FeAl}_2O_4$ ,  $n\text{-CrFe}_2O_4$ , and  $n\text{-CuFe}_2O_4$  compounds of the normal spinel and  $i\text{-NiFe}_2O_4$ ,  $i\text{-AlFe}_2O_4$ ,  $i\text{-CrFe}_2O_4$ , and  $i\text{-CuFe}_2O_4$  compounds of the inverse spinel, as well as to understand the differences in their thermal and mechanical properties. We calculated the normal spinel and inverse spinel compounds using different models. The normal spinel compound reflected a cubic (space group:  $Fd\text{-}3m$ ) structure with formula  $AB_2O_4$ . In contrast, the inverse spinel compound reflected an orthorhombic (space group:  $Imma$ ) structure, in which the pair strains were uniformly oriented relative to the cubic structure [20,21].

## 2. Computational Methods

First-principles calculations were performed using the Vienna Ab initio Simulation Package (VASP) [22,23]. The exchange and correlation interactions were described using the generalized gradient approximation (GGA) formulated by Perdew, Burke, and Ernzerhof (PBE) [24,25]. Furthermore, we used the GGA with the Hubbard U parameterization method (GGA + U) to describe the exchange-correlation potential [26]. To integrate the Brillouin zone, we used the Monkhorst pack [27] for the normal spinel compound (cubic) of  $n\text{-NiFe}_2O_4$ ,  $n\text{-FeAl}_2O_4$ ,  $n\text{-CrFe}_2O_4$ , and  $n\text{-CuFe}_2O_4$ , and the inverse spinel compound (orthorhombic) of  $i\text{-NiFe}_2O_4$ ,  $i\text{-AlFe}_2O_4$ ,  $i\text{-CrFe}_2O_4$ , and  $i\text{-CuFe}_2O_4$  (Figure 1a–h). An  $11 \times 11 \times 11$  k-point mesh was used for the structural optimization, total energy, and density of states calculations, whereas a  $7 \times 7 \times 7$  k-point mesh was used to calculate the elastic constants. The electronic structures were calculated using single-point energy calculations of the optimized models for normal and inverse spinel compounds. These k-points were obtained from the k-point convergence test, shown in Figure 1i,j. Accurate results were obtained using a high-energy cutoff of 500 eV with a precise energy convergence of 0.015 eV/Å. Integration was conducted using the tetrahedron method with Bloch corrections. All calculations were performed with spin-polarization. The Hubbard onsite correction term U parameters of the relevant elements for the d electrons are as follows: Fe = 4.0 eV, Ni = 6.0 eV, Cr = 3.5 eV, and Cu = 4.0 eV [28–30]. The elastic constants of the spinel compounds were estimated using the stress–strain method. Three different independent symmetry elements ( $C_{11}$ ,  $C_{12}$ , and  $C_{44}$ ) exist for cubic crystals. Meanwhile, orthorhombic symmetry possesses nine different independent elastic constants ( $C_{11}$ ,  $C_{12}$ ,  $C_{13}$ ,  $C_{22}$ ,  $C_{23}$ ,  $C_{33}$ ,  $C_{44}$ ,  $C_{55}$ , and  $C_{66}$ ) [31]. The elastic properties of the ordered normal and inverse spinel compounds were calculated using the following equations [32,33]:

$$B_v = B_R = 1/3(C_{11} + 2C_{12}) \quad (1)$$

$$G_v = 1/5(C_{11} - C_{12} + 3C_{44}) \quad (2)$$

$$G_R = 5(C_{11} - C_{12})C_{44}/4C_{44} + 3(C_{11} - C_{12}) \quad (3)$$

$$B_v = 1/9(C_{11} + C_{22} + C_{33} + 2C_{12} + 2C_{13} + 2C_{23}) \quad (4)$$

$$G_v = 1/15[+C_{22} + C_{33} + 3C_{44} + 3C_{55} + 3C_{66} - (C_{12} + C_{13} + C_{23})] \quad (5)$$

$$B_R = [C_{11}(C_{22} + C_{33} - 2C_{23}) + C_{22}(C_{33} - 2C_{13}) - 2C_{33}C_{12} + C_{12}(2C_{23} - C_{12}) + C_{13}(2C_{12} - C_{13}) + C_{23}]^{-1} \quad (6)$$

$$G_R = 15\{4[C_{11}(C_{22} + C_{33} - C_{23}) + C_{22}(C_{33} + C_{13}) + C_{33}C_{12} - C_{12}(C_{12} + C_{23}) - C_{13}(C_{13} + C_{12}) - C_{23}(C_{23} + C_{13})]/C_{13}(C_{12}C_{23} - C_{13}C_{22} + C_{23}(C_{12}C_{13} - C_{23}C_{11}) + C_{33}(C_{11}C_{22} - C_{12}^2 + 3(1/C_{44} + 1/C_{55} + 1/C_{66}))\}^{-1} \quad (7)$$

$$E = 9BG/(3B + G) \quad (8)$$

where  $B$ ,  $G$ , and  $E$  are the bulk, shear, and Young's moduli, respectively;  $V$ ,  $R$ , and  $VRH$  represent the Voigt, Reuss, and Voigt–Reuss–Hill approximations, respectively. Additionally, the formulations employed in the present study are listed in Section 3.

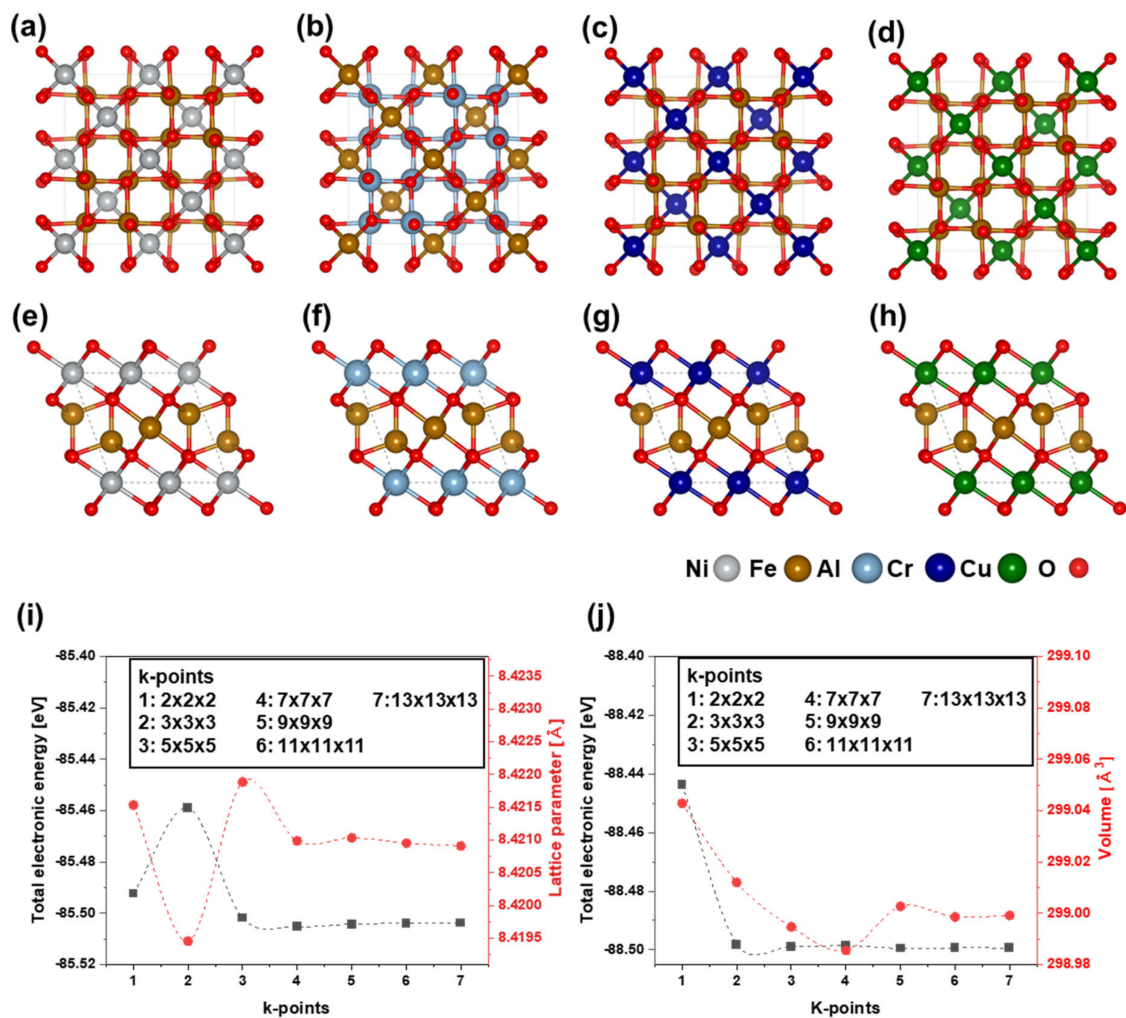


**Figure 1.** Structure models of normal ( $Fd-3m$ , cubic) and inverse ( $Imma$ , orthorhombic) spinel compound for (a) n-NiFe<sub>2</sub>O<sub>4</sub>, (b) n-FeAl<sub>2</sub>O<sub>4</sub>, (c) n-CrFe<sub>2</sub>O<sub>4</sub>, (d) n-CuFe<sub>2</sub>O<sub>4</sub>, (e) i-NiFe<sub>2</sub>O<sub>4</sub>, (f) i-AlFe<sub>2</sub>O<sub>4</sub>, (g) i-CrFe<sub>2</sub>O<sub>4</sub>, and (h) i-CuFe<sub>2</sub>O<sub>4</sub>. K-point convergence test: (i) variations in total electronic energy and lattice parameter for normal spinel compound model; (j) variations in total electronic energy and volume for inverse spinel compound model.

### 3. Results and Discussion

The equilibrium lattice parameters, formation energies, and cohesive energies of the normal and inverse spinel compounds are listed in Table 1 [34–39]. To evaluate the structural stability, the formation energy ( $E_{form}$ ) and cohesive energy ( $E_{coh}$ ) of the spinel compounds were calculated as follows [40]:

$$E_{Form} = \left[ E_{tot}^{ABO} - E_{solid}^A \times m - E_{solid}^B \times n - 1/2 E_{gas}^{O_2} \times 4 \right] / (m + n + 4) \quad (9)$$

$$E_{coh} = \left[ E_{tot}^{ABO} - E_{atom}^A \times m - E_{atom}^B \times n - E_{atom}^O \times 4 \right] / (m + n + 4) \quad (10)$$

where  $m$  and  $n$  refer to the numbers of Fe, Ni, Al, Cr, Cu, and O atoms.  $E_{solid}^A$  and  $E_{solid}^B$  are the average energies per atom with Fe, Ni, Al, Cr, and Cu in the solid states;  $E_{atom}^A$  and  $E_{atom}^B$  are the energies of the Fe, Ni, Al, Cr, and Cu free atoms in the cell lattice;  $E_{total}^{ABO}$  is the total energy of the  $A_x(B_2)_yO_4$  and  $B_x(AB)_yO_4$  spinel compounds. It was observed that the values of the lattice parameters for all calculated stable spinel compounds were consistent with the experimental and other theoretical values. The results show that the formation energy and cohesive energy of both the normal and inverse spinel compounds were negative. The inverse spinel compound indicated a lower formation energy than the normal spinel compound. Therefore, it was expected that the inverse spinel phase would require a lower energy than the general spinel phase during oxide scale formation. In particular, the oxide scale formation rate of the *i*-AlFe<sub>2</sub>O<sub>4</sub> spinel compound is expected to be high. Higher cohesive energies were observed in all normal spinel compounds, which indicated a decline in bonding strength. In addition, the lower the density of the spinel compound, the higher the possibility of peeling due to poor contact with the anode surface. Densities of normal and inverse spinel compounds were lower in the Al-containing compounds, *n*-FeAl<sub>2</sub>O<sub>4</sub> and *i*-AlFe<sub>2</sub>O<sub>4</sub>. The *n*-CuFe<sub>2</sub>O<sub>4</sub> and *i*-CuFe<sub>2</sub>O<sub>4</sub> compounds were shown to have high densities.

**Table 1.** Calculated lattice parameters ( $a_0$ ,  $b_0$ , and  $c_0$  in Å), formation energy ( $E_{form}$  in eV/atom), cohesive energy ( $E_{coh}$  in eV), and volume ( $V_0$  in Å<sup>3</sup>). For comparison, previous experimental and other theoretical values are listed.

Compound	Spinel Type	$a_0$	$b_0$	$c_0$	$E_{form}$	$E_{coh}$	$V_0$
NiFe <sub>2</sub> O <sub>4</sub>	Normal	8.420	8.420	8.420	−0.951	−1.291	597.01
		8.426 <sup>a</sup>	8.426 <sup>a</sup>	8.426 <sup>a</sup>	-	-	-
		8.339 <sup>b</sup>	8.339 <sup>b</sup>	8.339 <sup>b</sup>	-	-	-
NiFe <sub>2</sub> O <sub>4</sub>	Inverse	5.937	5.982	8.417	−2.008	−2.691	298.98
FeAl <sub>2</sub> O <sub>4</sub>	Normal	8.226	8.226	8.226	−1.334	−1.624	556.77
		8.230 <sup>c</sup>	8.230 <sup>c</sup>	8.230 <sup>c</sup>	-	-	-
		8.119 <sup>d</sup>	8.119 <sup>d</sup>	8.119 <sup>d</sup>	-	-	-
AlFe <sub>2</sub> O <sub>4</sub>	Inverse	5.838	5.912	8.497	−2.575	−3.154	301.41
CrFe <sub>2</sub> O <sub>4</sub>	Normal	8.510	8.510	8.510	−1.119	−1.441	614.21
CrFe <sub>2</sub> O <sub>4</sub>	Inverse	6.019	5.993	8.678	−2.328	−2.971	313.10
CuFe <sub>2</sub> O <sub>4</sub>	Normal	8.466	8.466	8.466	−0.963	−1.274	606.76
		8.465 <sup>e</sup>	8.465 <sup>e</sup>	8.465 <sup>e</sup>	-	-	-
CuFe <sub>2</sub> O <sub>4</sub>	Inverse	8.367 <sup>f</sup>	8.367 <sup>f</sup>	8.367 <sup>f</sup>	-	-	-
		5.829	5.907	8.846	−1.936	−2.559	304.66

<sup>a</sup> Ref. [34] calculation data. <sup>b</sup> Ref. [35] experimental data. <sup>c</sup> Ref. [36] calculation data. <sup>d</sup> Ref. [37] experimental data. <sup>e</sup> Ref. [38] calculation data. <sup>f</sup> Ref. [39] experimental data.

The equilibrium bulk ( $B$ ), shear ( $G$ ), Young's moduli ( $E$ ), Poisson's ratio ( $\nu$ ), Pugh's constant ( $G/B$ ), universal anisotropy index ( $A^U$ ), and empirical hardness of the normal and inverse spinel compounds are listed in Table 2 [34,41]. The bulk moduli of *i*-NiFe<sub>2</sub>O<sub>4</sub> and *n*-FeAl<sub>2</sub>O<sub>4</sub> were larger, which indicate that they have a greater resistance to deformation

than the other compounds. Similarly, the shear and Young's moduli of  $i\text{-NiFe}_2\text{O}_4$ ,  $n\text{-FeAl}_2\text{O}_4$ , and  $i\text{-AlFe}_2\text{O}_4$  were higher than those of the other spinel compounds. These results show that  $i\text{-NiFe}_2\text{O}_4$ ,  $n\text{-FeAl}_2\text{O}_4$  and  $i\text{-AlFe}_2\text{O}_4$  are not only more resistant to shear deformation, but can also withstand longitudinal deformation better than other spinel compounds. By contrast, the bulk, shear, and Young's moduli values of the  $n\text{-CrFe}_2\text{O}_4$ ,  $i\text{-CrFe}_2\text{O}_4$ ,  $n\text{-CuFe}_2\text{O}_4$ , and  $i\text{-CuFe}_2\text{O}_4$  compounds were lower than those of the other two compounds. In particular,  $n\text{-CuFe}_2\text{O}_4$  exhibited an extremely low shear and Young's moduli. Therefore,  $n\text{-FeAl}_2\text{O}_4$  and  $i\text{-AlFe}_2\text{O}_4$  are expected to exhibit excellent deformation against external stress, except for the  $\text{NiFe}_2\text{O}_4$  compound oxide scale typically formed in Fe–Ni–M anodes.

**Table 2.** Calculated mechanical properties of two types of spinel compounds: bulk modulus ( $B$  in GPa), shear modulus ( $G$  in GPa), Young's modulus ( $E$  in GPa), Poisson's ratio ( $\nu$ ), Pugh's constant ( $G/B$ ), universal anisotropy index ( $A^U$ ), and empirical hardness ( $H_V$  in GPa) for  $\text{NiFe}_2\text{O}_4$  and  $\text{FeAl}_2\text{O}_4$  with normal and inverse spinel compounds.

Compound	Spinel Type	$B$	$G$	$E$	$\nu$	$G/B$	$H_V$	$A^U$
$\text{NiFe}_2\text{O}_4$	normal	161.41	47.74	130.15	0.36	0.29	3.91	1.64
$\text{NiFe}_2\text{O}_4$	inverse	177.1 <sup>a</sup>	-	-	-	-	-	-
$\text{NiFe}_2\text{O}_4$	inverse	170.69	61.54	164.76	0.34	0.36	5.57	0.69
$\text{FeAl}_2\text{O}_4$	normal	184.79	64.93	173.51	0.34	0.35	6.22	2.98
$\text{FeAl}_2\text{O}_4$	inverse	172.4 <sup>b</sup>	56.9 <sup>b</sup>	153.8 <sup>b</sup>	-	-	-	-
$\text{AlFe}_2\text{O}_4$	inverse	159.64	61.86	164.19	0.32	0.38	6.21	1.11
$\text{CrFe}_2\text{O}_4$	normal	155.03	48.88	132.63	0.35	0.31	4.07	0.73
$\text{CrFe}_2\text{O}_4$	inverse	164.74	55.03	148.33	0.35	0.33	4.92	1.49
$\text{CuFe}_2\text{O}_4$	normal	152.78	27.89	77.82	0.41	0.18	1.85	9.25
$\text{CuFe}_2\text{O}_4$	inverse	156.69	49.72	134.81	0.35	0.31	4.23	1.11

<sup>a</sup> Ref. [34] calculation. <sup>b</sup> Ref. [40] calculation.

The results reveal that the Poisson's ratios of the spinel phases were between  $\nu = 0.25$  and 0.33, indicating ionic and metallic bonding in all atoms of the spinel compound. The Poisson's ratio is an index that describes the directionality of chemical bond; it is  $\nu = 0.1$ , for covalent bonds,  $\nu = 0.25$  for ionic bonds, and  $\nu = 0.33$  for metallic bonds [42]:

$$\nu = (3B - 2G)/2(3B + G) \quad (11)$$

In addition, the ductile/brittle behavior of spinel compounds was also considered using Pugh's constant  $G/B$  [43]. A compound exhibits ductility when  $G/B$  is lower than 0.57; otherwise, it is brittle. The  $G/B$  value calculated for all spinel compounds was less than 0.57, indicating a high ductility; this is consistent with the Poisson's ratio calculated previously. This indicates that all spinel compounds have high thermal shock resistance. Furthermore, it indicates that cracks progress slowly when plastic deformation occurs. Hardness is an important parameter for evaluating the wear behavior of materials [44,45]. Therefore, the hardness of the inert anode materials must be investigated. Hardness can be obtained using the Poisson's ratio and Young's modulus [46]. In this study, we used a relatively simple semi-empirical equation for hardness, as follows [47]:

$$H_V = 0.92k^{1.137}G^{0.708} \quad (12)$$

where,  $G$  is the shear modulus, and  $k$  is Pugh's constant ( $G/B$ ). The results are consistent with the relationship between hardness and ductility. Therefore, we concluded that the hardness values calculated in this study were reliable. In particular,  $n\text{-FeAl}_2\text{O}_4$  and  $i\text{-AlFe}_2\text{O}_4$  indicated the highest values of hardness, i.e., 6.22 and 6.21, respectively. As such, they were expected to exhibit excellent durability and few cracks when forming an oxide scale.

The universal anisotropy index ( $A^U$ ) determines the transfer probability of microcracks and the structural stability of a material [48]. A material is elastically isotropic when it satisfies  $A^U = 0$ ; otherwise, it is elastically anisotropic. To characterize elastic anisotropy, we adopted the universal anisotropy index proposed for all crystal systems, as follows [49]:

$$A^U = 5G_v/G_R + B_v/B_R - 6 \geq 0 \quad (13)$$

where  $G$  is the shear modulus;  $B$  is the bulk modulus; and subscripts,  $V$  and  $R$ , denote the Voigt and Reuss averages, respectively. Our calculations show that the  $A^U$  values deviated from zero, indicating that both compounds were anisotropic. Furthermore, it was emphasized that these compounds were more likely to develop structural defects or microcracks during their growth into oxide scales. The ceramics should preferably be isotropic; otherwise, they will deform preferentially in a specific direction. In particular,  $n\text{-CuFe}_2\text{O}_4$  exhibited a greater anisotropy than the other compounds; therefore, its oxide scale was expected to fracture easily.

Nevertheless, these factors do not contribute sufficiently to the complete description of the elastic anisotropic behavior of the crystals. The orientation dependence of the Young's modulus is typically employed to analyze the elastic anisotropy of the crystals [50]. The elastic stress field is controlled by elastic anisotropy, which dominates the initial slip system. Therefore, the illustration of elastic anisotropy is important for predicting the stress field evolution as a function of the crystal orientation [51]. Calculating the elastic anisotropy of spinel compounds is important for understanding these properties and identifying mechanisms that will improve their durability. To further investigate the anisotropic features of the spinel compound, a three-dimensional (3D) surface representation of the elastic anisotropy of the crystal was created. For cubic and orthorhombic crystals, the Young's modulus in any orientation is expressed as [52,53]:

$$1/E = S_{11} - 2(S_{11} - S_{12} - S_{44}/2)(l_1^2 l_2^2 + l_2^2 l_3^2 + l_1^2 l_3^2) \quad (14)$$

$$1/E = S_{11}l_1^4 + (2S_{12} + S_{66})l_1^2 l_2^2 + S_{22}l_1^4 + (2S_{23} + S_{44})l_2^2 l_3^2 + S_{33}l_3^4 + (2S_{13} + S_{55})l_1^2 l_3^2 \quad (15)$$

where  $l_1$ ,  $l_2$ , and  $l_3$  are direction cosines with respect to the  $a$ ,  $b$ , and  $c$  directions of the lattice, respectively. The spatial 3D surface representation of the Young's modulus is shown in Figure 2a–h. Young's modulus surfaces are perfectly spherical for isotropic crystals, but not for normal and inverse spinel compounds. This shows that the normal and inverse spinels exhibit elastic anisotropy. Furthermore, the Young's moduli of the normal and inverse spinel compounds in the normal direction of three low-index crystal planes  $\{100\}$ ,  $\{110\}$ , and  $\{111\}$  were calculated. The equations for normal directions of the planes are as follows [51]:

$$1/E_{hkl} = S_{11} - 2S_0[(hk)^2 + (hl)^2 + (lk)^2 / (h^2 + k^2 + l^2)^2] \quad (16)$$

$$S_0 = S_{11} - S_{12} - 1/2S_{44} \quad (17)$$

The corresponding calculation results are listed in Table 3. The calculated normal and inverse spinel compounds showed different Young's moduli values depending on the plane direction. The general spinel compounds indicated the highest stiffness in the  $\{111\}$  direction, regardless of the composition. The inverse spinel compounds indicated the highest stiffness in the  $\{100\}$  direction, regardless of the composition. In terms of  $n\text{-CuFe}_2\text{O}_4$ , the Young's moduli differed significantly depending on the plane direction. The calculated minimum and maximum values of the Young's modulus were 19.07 and 171.6 GPa for the  $\{100\}$  plane; 47.87 and 144.33 GPa for the  $\{110\}$  plane, and 54.57 and 278.4 GPa for the  $\{111\}$  plane. In general, spinel compounds with a high rigidity along the plane direction were indicated as  $n\text{-NiFe}_2\text{O}_4$  in  $\{100\}$ ,  $n\text{-FeAl}_2\text{O}_4$  in  $\{110\}$ , and  $n\text{-CuFe}_2\text{O}_4$  in  $\{111\}$ .

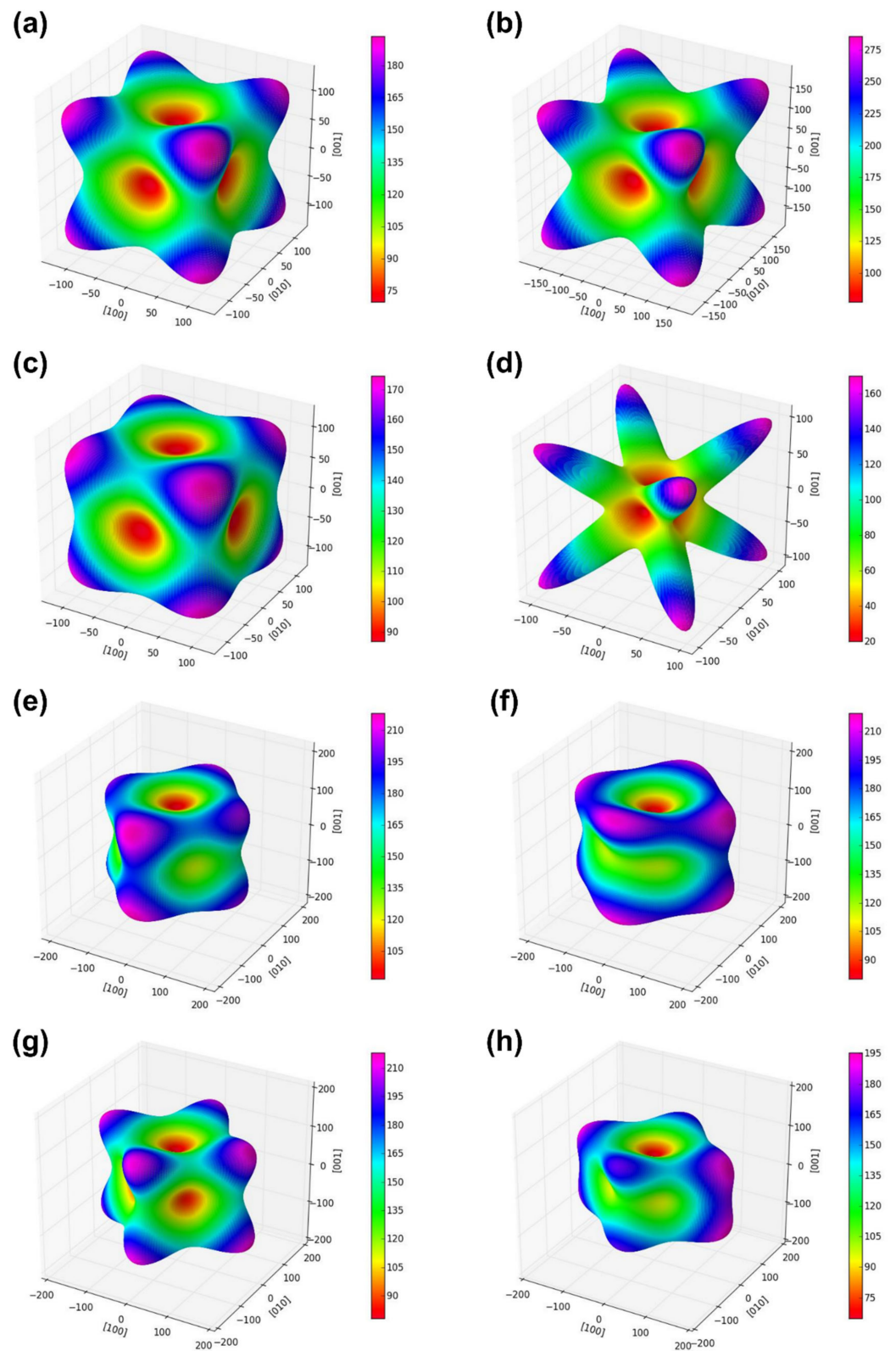


**Figure 2.** Directional dependence of Young's modulus for spinel compounds (a) n-NiFe<sub>2</sub>O<sub>4</sub>, (b) n-FeAl<sub>2</sub>O<sub>4</sub>, (c) n-CrFe<sub>2</sub>O<sub>4</sub>, (d) n-CuFe<sub>2</sub>O<sub>4</sub>, (e) i-NiFe<sub>2</sub>O<sub>4</sub>, (f) i-AlFe<sub>2</sub>O<sub>4</sub>, (g) i-CrFe<sub>2</sub>O<sub>4</sub>, and (h) i-CuFe<sub>2</sub>O<sub>4</sub>.

**Table 3.** Calculated values of Young's modulus ( $E_{hkl}$  in GPa) along normal directions of planes {100}, {110}, and {111}.

Compound	Spinel Type	{100}	{110}	{111}
NiFe <sub>2</sub> O <sub>4</sub>	normal	61.06	118.53	148.19
NiFe <sub>2</sub> O <sub>4</sub>	inverse	171.60	57.58	65.50
FeAl <sub>2</sub> O <sub>4</sub>	normal	67.94	144.33	200.82
AlFe <sub>2</sub> O <sub>4</sub>	inverse	159.69	55.72	68.00
CrFe <sub>2</sub> O <sub>4</sub>	normal	73.22	111.76	129.65
CrFe <sub>2</sub> O <sub>4</sub>	inverse	164.75	47.87	62.20
CuFe <sub>2</sub> O <sub>4</sub>	normal	19.07	109.96	278.40
CuFe <sub>2</sub> O <sub>4</sub>	inverse	158.94	44.86	54.57

Generally, the Debye temperature ( $\theta_D$ ) is a fundamental parameter associated with a number of physical properties of materials, including their elastic constants, specific heat, chemical bonding, and melting point [54,55]. Excitation due to low-temperature vibrations occurs only in acoustic vibrations. The following equation was used to estimate the magnitude of the  $\theta_D$  at the average speed of sound [55]:

$$\theta_D = h/k_B [3n/4\pi(N_A\rho/M)]^{1/3} v_m \quad (18)$$

where  $M$  is the mean molecular weight,  $n$  the total number of atoms in the formula unit,  $\rho$  the mass density,  $h$  the Plank constant,  $k_B$  the Boltzmann constant, and  $N_A$  the Avogadro number. For polycrystalline materials, the average velocity of sound  $v_m$  is expressed as [9]:

$$v_m = [1/3(1/v_l^3 + 2/v_t^3)]^{-1/3} \quad (19)$$

$$v_l = \sqrt{(B + (4/3)G)/\rho} \quad (20)$$

$$v_t = \sqrt{G/\rho} \quad (21)$$

where  $v_l$  and  $v_t$  represent the longitudinal and transverse sound velocities in anisotropic materials, respectively. They can be determined in terms of the bulk modulus  $B$  and shear modulus  $G$  [56]. For crystal structures,  $\theta_D$  defines the highest temperature of the material for the normal vibrational mode, specific heat, and melting temperature. As shown in Table 4, the n-FeAl<sub>2</sub>O<sub>4</sub> and i-AlFe<sub>2</sub>O<sub>4</sub> spinels had the largest  $\theta_D$  values of 617.7 K and 733.2 K, respectively. The calculated average sound velocities of these n-FeAl<sub>2</sub>O<sub>4</sub> and i-AlFe<sub>2</sub>O<sub>4</sub> compounds were relatively large, because they had large elastic moduli and small densities. The  $v_l$  and  $v_t$  values are associated with the density, shear modulus, and bulk modulus. The high volume leads to the formation of thick spinel oxide scale, which reduces the contact with the electrolyte, thereby reducing the electrochemical properties. In contrast, when thin spinel oxide scales are formed, the electrochemical properties are increased but the mechanical behavior is decreased. It is expected that normal spinel oxide scales are bulkier than inverse spinel oxide scales and form thick oxide scales, whereas inverse spinel oxide scales are expected to form thin oxide scales. When comparing normal and inverse spinel of the same element, n-FeAl<sub>2</sub>O<sub>4</sub> and i-AlFe<sub>2</sub>O<sub>4</sub> compounds are expected to form the most ideal oxide scale. However, no experimental or theoretical evidence for comparing our results in terms of density,  $\theta_D$ , and elastic wave is available in the literature.

**Table 4.** Calculated thermal properties: density ( $\rho$  in g/cm<sup>3</sup>), transverse ( $v_t$  in m/s), longitudinal ( $v_l$  in m/s), mean speed of sound ( $v_m$  in m/s), and Debye temperature ( $\theta_D$  in K).

Compound	Spinel Type	$\rho$	$v_t$	$v_l$	$V_m$	$\theta_D$
NiFe <sub>2</sub> O <sub>4</sub>	normal	5.215	3067	6659	3456	463.2
NiFe <sub>2</sub> O <sub>4</sub>	inverse	5.207	3477	7047	3904	523.8
FeAl <sub>2</sub> O <sub>4</sub>	normal	4.147	4003	8183	4496	617.7
AlFe <sub>2</sub> O <sub>4</sub>	inverse	4.466	3725	7370	4176	562.8
CrFe <sub>2</sub> O <sub>4</sub>	normal	4.925	3205	6802	3607	477.8
CrFe <sub>2</sub> O <sub>4</sub>	inverse	4.830	3418	7109	3842	507.3
CuFe <sub>2</sub> O <sub>4</sub>	normal	5.238	2329	6079	2641	353.1
CuFe <sub>2</sub> O <sub>4</sub>	inverse	5.216	3134	6638	3527	469.1

To investigate the causes of the mechanical and electrochemical properties of normal and inverse spinel compounds, we calculated and compared their electronic structures. Figure 3 shows the calculated total density of states (TDOS) and partial density of states (PDOS) of (a) n-Fe<sub>2</sub>NiO<sub>4</sub>, (b) i-Fe<sub>2</sub>NiO<sub>4</sub>, (c) n-Fe<sub>2</sub>AlO<sub>4</sub>, (d) i-AlFe<sub>2</sub>O<sub>4</sub>, (e) n-CrFe<sub>2</sub>O<sub>4</sub>, (f) i-CrFe<sub>2</sub>O<sub>4</sub>, (g) n-CuFe<sub>2</sub>O<sub>4</sub>, and (h) i-CuFe<sub>2</sub>O<sub>4</sub> spinel compounds. The energy level 0 eV on the x-axis represents the Fermi level of the spinel compound. Figure 3a,b shows that Fe-3d orbital is separated into t<sub>2g</sub>-up and e<sub>g</sub>-up to generate a valence band using O-2p orbital and conduction in Fe-3d orbital [57]. Figure 3c,d shows that the high peaks near the Fermi level correspond to Fe 3d states. In addition, in the Valence band, Fe-3d and Al-3p states contribute to the formation of the highest peak. The high peak in the conduction band is caused by the Fe-3d states [58]. As shown in the figure, majority spins were observed in the valence band and minority spins in the conduction band. Figure 3e,f show shifts in the Fermi level of the 3d state peaks of Fe and Cr cations between the two spin directions for this compound. As a result, the 3d states of the Fe and Cr transition metals were confirmed as the possible cause of magnetism. The highest peak in the valence band is due to Fe-3d states. The highest peak in the conduction band is caused by Fe-3d states. In particular, it was observed that the Fe-3d and Cr-3d states overlapped in the peak with a high electron density. Figure 3g,h shows that the peak at the Fermi level was observed to be connected with the Cr-3d state. The highest peak in the valence band is caused by the Fe-3d and Cr-3d states, and the conduction band is caused by the Fe-3d states. On the other hand, in the case of i-CuFe<sub>2</sub>O<sub>4</sub>, there was no large peak near the Fermi level. In particular, minority Cr-3d states were observed in the conduction band. As a result, it was observed that the transition metal elements were determined by 3d states, and Al and O elements were determined by 2p states.

The spinel oxide scales i-NiFe<sub>2</sub>O<sub>4</sub>, i-AlFe<sub>2</sub>O<sub>4</sub>, n-CrFe<sub>2</sub>O<sub>4</sub>, i-CrFe<sub>2</sub>O<sub>4</sub>, and i-CuFe<sub>2</sub>O<sub>4</sub> exhibit insulator properties. In contrast, n-NiFe<sub>2</sub>O<sub>4</sub>, n-FeAl<sub>2</sub>O<sub>4</sub>, and n-CuFe<sub>2</sub>O<sub>4</sub> exhibit conductor properties. As many densities of states near the Fermi level contribute to charge storage, the n-NiFe<sub>2</sub>O<sub>4</sub>, n-FeAl<sub>2</sub>O<sub>4</sub>, and n-CuFe<sub>2</sub>O<sub>4</sub> spinel compounds should improve their electrochemical performance after they are formed in the scale [41]. In particular, the TDOS of NiFe<sub>2</sub>O<sub>4</sub> shows a strong peak in the spin-down state close to the Fermi energy level ( $\pm 0.2$  eV). Al-O bonds are ionic in nature. As Al atoms are replaced by Fe atoms, the charge density increases, forming Fe-O bonds with both ionicity and covalent properties [59]. Therefore, it is expected that the electrical conductivity properties of the n-NiFe<sub>2</sub>O<sub>4</sub> and n-FeAl<sub>2</sub>O<sub>4</sub> oxide scales will be excellent.

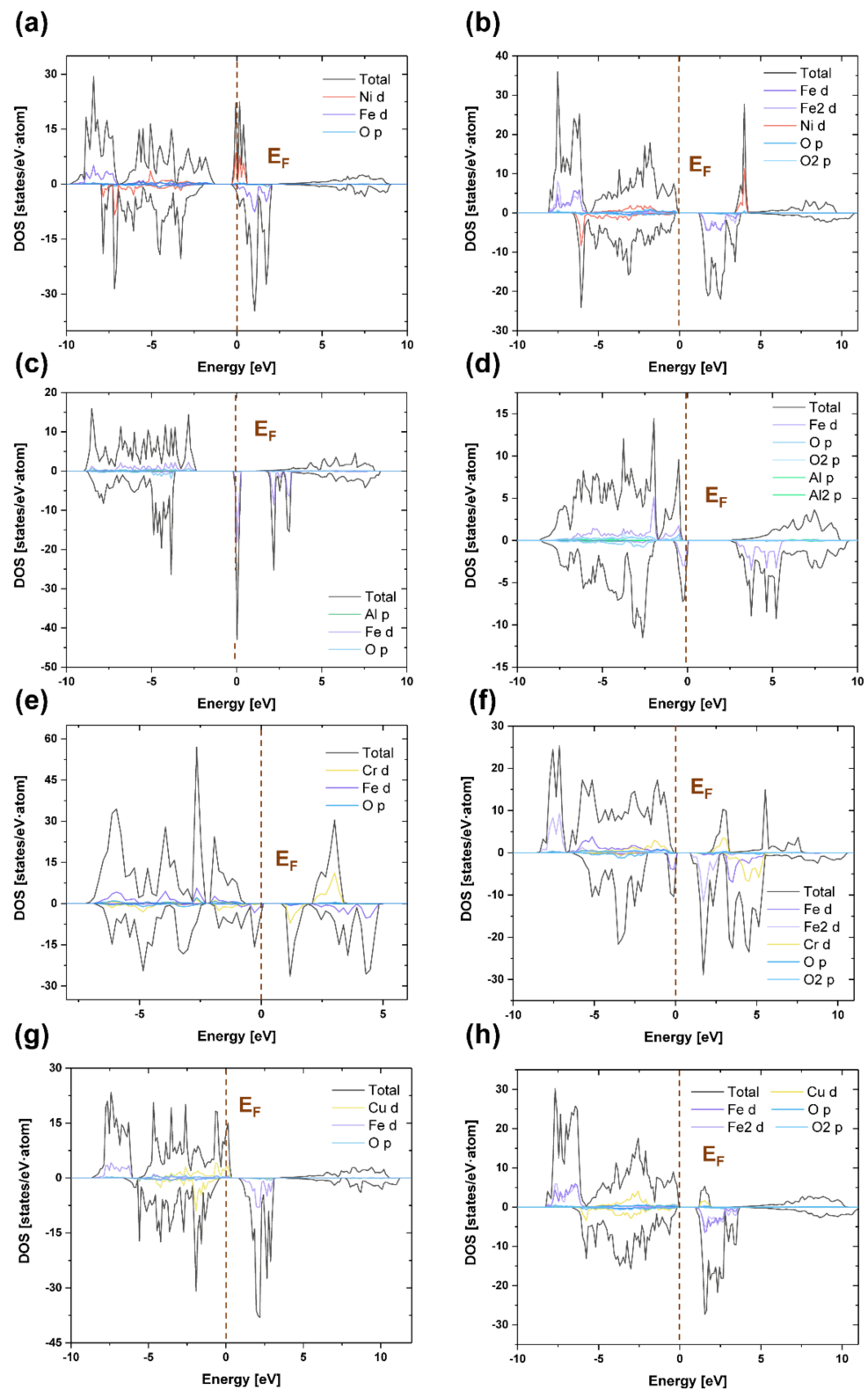


**Figure 3.** TDOS and PDOS of normal and inverse spinel compounds (a) n-NiFe<sub>2</sub>O<sub>4</sub>, (b) i-NiFe<sub>2</sub>O<sub>4</sub>, (c) n-FeAl<sub>2</sub>O<sub>4</sub>, (d) i-FeAl<sub>2</sub>O<sub>4</sub>, (e) n-CrFe<sub>2</sub>O<sub>4</sub>, (f) i-CrFe<sub>2</sub>O<sub>4</sub>, (g) n-CuFe<sub>2</sub>O<sub>4</sub>, and (h) i-CuFe<sub>2</sub>O<sub>4</sub>. The vertical dashed lines indicate the Fermi level.

The minimum thermal conductivities of the spinel compounds are shown in Figure 4. Thermal conductivity describes the diffusivity of heat flow via phonon transport in a temperature gradient. Crystalline materials typically exhibit four distinct regions in the

thermal conductivity–temperature curve. To investigate the behavior at high temperatures, the last of the four areas must be emphasized, i.e., the high-temperature region that exceeds  $\theta_D$ , where the thermal conductivity exhibits a minimum value. The minimum thermal conductivity was calculated using Clarke’s model, which can be expressed as [60,61]:

$$k_{min} = 0.87k_B\overline{M}_a^{-2/3}E^{1/2}\rho^{1/6}, \overline{M}_a = [M/(m \cdot N_A)] \quad (22)$$

where  $K_B$  is the Boltzmann constant,  $\rho$  is the density,  $E$  is the Young’s modulus,  $N_A$  is the Avogadro number,  $M$  is the molar mass,  $m$  is the total number of atoms per formula, and  $\overline{M}_a$  is the average mass per atom. The thermal conductivity of solid materials varies with temperature and pressure because the phonon means that the free paths and vibration properties of the material depend on the temperature and pressure [62]. At high temperatures, solid materials converge to the minimum value of thermal conductivity, as suggested by Clarke. The minimum thermal conductivity is proportional to the mean acoustic velocity, and this velocity is affected by the rigidity of the material. Therefore, the results of this study show the minimum thermal conductivity in the order  $n\text{-CuFe}_2\text{O}_4 > n\text{-CrFe}_2\text{O}_4 > i\text{-CuFe}_2\text{O}_4 > i\text{-CrFe}_2\text{O}_4 > n\text{-NiFe}_2\text{O}_4 > i\text{-FeAl}_2\text{O}_4 > i\text{-NiFe}_2\text{O}_4 > n\text{-FeAl}_2\text{O}_4$ . According to the obtained mechanical properties and thermal conductivity,  $n\text{-FeAl}_2\text{O}_4$  and  $i\text{-AlFe}_2\text{O}_4$  exhibited mechanical stability and a low thermal conductivity. It is beneficial to provide the physical property information when  $n\text{-FeAl}_2\text{O}_4$  and  $i\text{-AlFe}_2\text{O}_4$  are regarded as potential candidates for inert anode oxide scales.

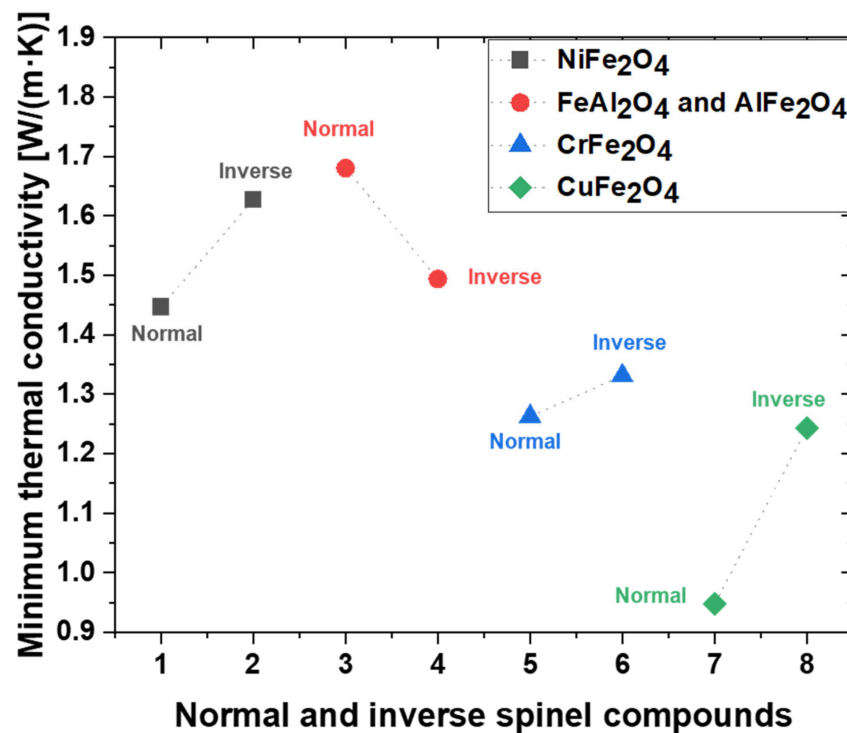


Figure 4. Minimum thermal conductivity ( $K_{min}$ ) of normal and inverse spinel compound.

Figure 5 shows the measured thermal expansion coefficients of the normal and inverse spinel compounds. The coefficient of thermal expansion is an important factor that affects non-uniform epitaxial growth. This is because the significant difference in the coefficient of thermal expansion between dissimilar materials results in defects such as cracks and mismatch dislocations at the boundary [63,64]. The effect of temperature was analyzed using the Debye–Grüneisen model [65,66]. Investigations of other  $\text{NiFe}_2\text{O}_4$  spinel compounds indicated comparable values between  $11\text{--}18 \times 10^{-6} \text{ K}^{-1}$  [67]. This value is consistent with the experimental data within 10% between 275 and 400 K, but significantly (15–16%) overestimates the measured expansion above this temperature. The possible reason for the

difference is that the anharmonicity correction of the Debye–Grüneisen model is too large to fit the experimental values. In addition, several different ferrite spinels with  $\text{NiFe}_2\text{O}_4$  were investigated in other studies, all of which indicate expansion at rates of  $7\text{--}13 \times 10^{-6} \text{ K}^{-1}$  at 1000 K [68]. This indicates that all of the normal and inverse spinel compounds investigated were overestimated. This deviation is expected because the calculation was performed on a perfect crystal, whereas the measured values are dependent on the purity of the sample, in which impurities, defects, and grain boundaries may be present.

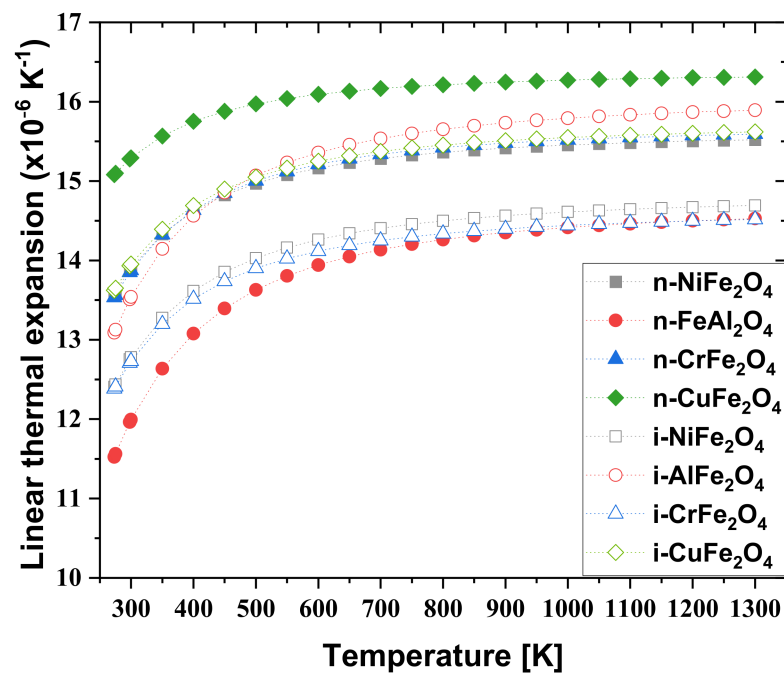


Figure 5. Comparison of calculated thermal expansion coefficients of normal and inverse spinel compound.

#### 4. Conclusions

We investigated the mechanical and thermal properties of normal and inverse spinel ( $\text{NiFe}_2\text{O}_4$ ,  $\text{FeAl}_2\text{O}_4$ ,  $\text{AlFe}_2\text{O}_4$ ,  $\text{CrFe}_2\text{O}_4$ , and  $\text{CuFe}_2\text{O}_4$ ) compounds using first-principles calculations via the GGA + U approach. In particular,  $\text{n-CuFe}_2\text{O}_4$  demonstrated the lowest compression resistance and theoretical hardness, whereas  $\text{n-FeAl}_2\text{O}_4$  exhibited the highest compression resistance and theoretical hardness. The trend of  $\theta_D$  was similar to the trends of shear and Young's moduli. Meanwhile, the trends for the mechanical and thermophysical properties correspond to the Poisson's ratio and Pugh's constants of our solid solution candidates. Mechanical anisotropy was described by both the universal anisotropy index and spatial 3D surfaces. The minimum thermal conductivity of  $\text{n-FeAl}_2\text{O}_4$  was the highest at  $1.680 \text{ W}/(\text{m}\cdot\text{K})$ , whereas that of  $\text{n-CuFe}_2\text{O}_4$  was the lowest at  $0.948 \text{ W}/(\text{m}\cdot\text{K})$ . According to our calculations,  $\text{NiFe}_2\text{O}_4$ ,  $\text{FeAl}_2\text{O}_4$ , and  $\text{AlFe}_2\text{O}_4$  are expected to exhibit excellent thermal shock resistance and anode surface adhesion. Therefore, good performances can be expected when an inert Fe–Ni–Al anode is used in the MSE process. We hope that this study will provide some insights for the further investigation of spinel compound oxide scales and the design of Fe–Ni-based inert anodes for electrolysis.

**Author Contributions:** Conceptualization, M.K.; methodology, M.K.; formal analysis, M.K.; investigation, J.K. (Jiwoo Kim); writing—original draft preparation, M.K.; writing—review and editing, J.K. (Jiwoong Kim); visualization, J.K. (Jiwoo Kim); supervision, J.K. (Jiwoong Kim); project administration, J.K. (Jungshin Kang); funding acquisition, J.K. (Jungshin Kang). All authors have read and agreed to the published version of the manuscript.

**Funding:** This research was supported by the National Research Council of Science and Technology (NST) grant by the Korea government (MSIT) (No. CRC-15-06-KIGAM) and the Korea Evaluation Institute of Industrial Technology funded by the Korean Ministry of Industry in Korea (Project No.: 20000970, 21-9805).

**Institutional Review Board Statement:** Not applicable.

**Informed Consent Statement:** Not applicable.

**Data Availability Statement:** Data sharing is not applicable.

**Conflicts of Interest:** The authors declare no conflict of interest.

## References

1. Cao, D.; Shi, Z.N.; Shi, D.; Xu, J.L.; Hu, X.W.; Wang, Z.W. Electrochemical Oxidation of Fe-Ni Alloys in Cryolite-Alumina Molten Salts at High Temperature. *J. Electrochem. Soc.* **2019**, *166*, E87–E96. [[CrossRef](#)]
2. Lee, T.H.; Okabe, T.H.; Lee, J.Y.; Kim, Y.M.; Kang, J. Molten Salt Electrolysis of Magnesium Oxide Using a Liquid-Metal Cathode for the Production of Magnesium Metal. *Metall. Mater. Trans. B* **2020**, *51*, 2993–3006. [[CrossRef](#)]
3. Haraldsson, J.; Johansson, M.T. Effects on primary energy use, greenhouse gas emissions and related costs from improving energy end-use efficiency in the electrolysis in primary aluminium production. *Energy Effic.* **2020**, *13*, 1299–1314. [[CrossRef](#)]
4. Paraskevas, D.; Kellens, K.; Van de Voorde, A.; Dewulf, W.; Duflou, J.R. Environmental Impact Analysis of Primary Aluminium Production at Country Level. *Procedia CIRP* **2016**, *40*, 209–213. [[CrossRef](#)]
5. Thonstad, J. On the Anode Gas Reactions in Aluminum Electrolysis, II. *J. Electrochem. Soc.* **1964**, *111*, 955–959. [[CrossRef](#)]
6. Lee, T.-H.; Park, H.; Lee, J.-Y.; Kim, Y.M.; Kang, J. Investigation of Electrowinning of Mg from MgO Using a Liquid Metal Cathode in MgF<sub>2</sub>-CaF<sub>2</sub>-NaF or MgF<sub>2</sub>-LiF Molten Salt. *J. Korean Inst. Met. Mater.* **2021**, *59*, 392–403. [[CrossRef](#)]
7. Lee, T.-H.; Okabe, T.H.; Lee, J.-Y.; Kim, Y.M.; Kang, J. Development of a novel electrolytic process for producing high-purity magnesium metal from magnesium oxide using a liquid tin cathode. *J. Magnes. Alloys* **2021**, *9*, 1644–1655. [[CrossRef](#)]
8. Lee, D.-H.; Jeoung, H.-J.; Lee, T.-H.; Yi, K.-W.; Lee, J.-Y.; Kim, Y.M.; Okabe, T.H.; Kang, J. Scale-Up Study of Molten Salt Electrolysis using Cu or Ag Cathode and Vacuum Distillation for the Production of High-Purity Mg Metal from MgO. *J. Sustain. Metall.* **2021**, *7*, 883–897. [[CrossRef](#)]
9. Wang, D.; Xiao, W. Inert anode development for high-temperature molten salts. In *Molten Salts Chemistry*; Elsevier: Amsterdam, The Netherlands, 2013; pp. 171–186.
10. Tian, Z.; Lai, Y.; Yang, S.; Li, J.; Hwang, J.-Y.; Liu, Y. Anodic Corrosion Behavior of NiFe<sub>2</sub>O<sub>4</sub>-Based Cermet in Na<sub>3</sub>AlF<sub>6</sub>-K<sub>3</sub>AlF<sub>6</sub>-AlF<sub>3</sub> for Aluminum Electrolysis. *Metall. Mater. Trans. B* **2015**, *46*, 1257–1261. [[CrossRef](#)]
11. Guan, P.; Liu, A.; Shi, Z.; Hu, X.; Wang, Z. Corrosion Behavior of Fe-Ni-Al Alloy Inert Anode in Cryolite Melts. *Metals* **2019**, *9*, 399. [[CrossRef](#)]
12. Olsen, E.; Thonstad, J. Nickel ferrite as inert anodes in aluminium electrolysis: Part II Material performance and long-term testing. *J. Appl. Electrochem.* **1999**, *29*, 301–311. [[CrossRef](#)]
13. Quan, C.; Deng, S.; Jiang, Y.; Jiang, C.; Shuai, M. Characteristics and high temperature oxidation behavior of Ni-Cr-Y<sub>2</sub>O<sub>3</sub> nanocomposite coating prepared by cathode plasma electrolytic deposition. *J. Alloys Compd.* **2019**, *793*, 170–178. [[CrossRef](#)]
14. Wei, W.; Geng, S.; Xie, D.; Wang, F. High temperature oxidation and corrosion behaviours of Ni-Fe-Cr alloys as inert anode for aluminum electrolysis. *Corros. Sci.* **2019**, *157*, 382–391. [[CrossRef](#)]
15. Chapman, V.; Welch, B.J.; Skyllas-Kazacos, M. Anodic behaviour of oxidised Ni-Fe alloys in cryolite-alumina melts. *Electrochim. Acta* **2011**, *56*, 1227–1238. [[CrossRef](#)]
16. Hossain, A.; Sarker, M.S.I.; Khan, M.K.R.; Rahman, M.M. Spin effect on electronic, magnetic and optical properties of spinel CoFe<sub>2</sub>O<sub>4</sub>: A DFT study. *Mater. Sci. Eng. B* **2020**, *253*, 114496–114501. [[CrossRef](#)]
17. Mo, S.D.; Ching, W.Y. Electronic structure of normal, inverse, and partially inverse spinels in the MgAl<sub>2</sub>O<sub>4</sub> system. *Phys. Rev. B Condens. Matter* **1996**, *54*, 16555–16561. [[CrossRef](#)]
18. Miller, A. Distribution of Cations in Spinel. *J. Appl. Phys.* **1959**, *30*, S24–S25. [[CrossRef](#)]
19. Guo, H.; Durham, J.L.; Brady, A.B.; Marschilok, A.C.; Takeuchi, E.S.; Takeuchi, K.J.; Liu, P. Essential Role of Spinel MgFe<sub>2</sub>O<sub>4</sub> Surfaces during Discharge. *J. Electrochem. Soc.* **2020**, *167*, 090506–090514. [[CrossRef](#)]
20. Ivanov, V.G.; Abrashev, M.V.; Iliev, M.N.; Gospodinov, M.M.; Meen, J.; Aroyo, M.I. Short-range B-site ordering in the inverse spinel ferrite NiFe<sub>2</sub>O<sub>4</sub>. *Phys. Rev. B* **2010**, *82*, 024104–024113. [[CrossRef](#)]
21. Liu, J.; Wang, X.; Borkiewicz, O.J.; Hu, E.; Xiao, R.J.; Chen, L.; Page, K. Unified View of the Local Cation-Ordered State in Inverse Spinel Oxides. *Inorg. Chem.* **2019**, *58*, 14389–14402. [[CrossRef](#)] [[PubMed](#)]
22. Hafner, J. Ab-initio simulations of materials using VASP: Density-functional theory and beyond. *J. Comput. Chem.* **2008**, *29*, 2044–2078. [[CrossRef](#)] [[PubMed](#)]
23. Kohn, W.; Sham, L.J. Self-Consistent Equations Including Exchange and Correlation Effects. *Phys. Rev.* **1965**, *140*, A1133–A1138. [[CrossRef](#)]
24. Ernzerhof, M.; Scuseria, G.E. Assessment of the Perdew–Burke–Ernzerhof exchange-correlation functional. *J. Chem. Phys.* **1999**, *110*, 5029–5036. [[CrossRef](#)]

25. Grimme, S. Semiempirical GGA-type density functional constructed with a long-range dispersion correction. *J. Comput. Chem.* **2006**, *27*, 1787–1799. [[CrossRef](#)] [[PubMed](#)]
26. Andriotis, A.N.; Sheetz, R.M.; Menon, M. LSDA + U method: A calculation of the U values at the Hartree-Fock level of approximation. *Phys. Rev. B* **2010**, *81*, 245103–245107. [[CrossRef](#)]
27. Monkhorst, H.J.; Pack, J.D. Special points for Brillouin-zone integrations. *Phys. Rev. B* **1976**, *13*, 5188–5192. [[CrossRef](#)]
28. Jain, A.; Hautier, G.; Ong, S.P.; Moore, C.J.; Fischer, C.C.; Persson, K.A.; Ceder, G. Formation enthalpies by mixing GGA and GGA+U calculations. *Phys. Rev. B* **2011**, *84*, 045115–045124. [[CrossRef](#)]
29. Zhou, F.; Cococcioni, M.; Marianetti, C.A.; Morgan, D.; Ceder, G. First-principles prediction of redox potentials in transition-metal compounds with LDA + U. *Phys. Rev. B* **2004**, *70*, 235121–235128. [[CrossRef](#)]
30. Dabaghmanesh, S.; Saniz, R.; Neyts, E.; Partoens, B. Sulfur-alloyed Cr<sub>2</sub>O<sub>3</sub>: A new p-type transparent conducting oxide host. *RSC Adv.* **2017**, *7*, 4453–4459. [[CrossRef](#)]
31. Reshak, A.H.; Jamal, M. DFT calculation for elastic constants of orthorhombic structure within WIEN2K code: A new package (ortho-elastic). *J. Alloys Compd.* **2012**, *543*, 147–151. [[CrossRef](#)]
32. Hill, R. The Elastic Behaviour of a Crystalline Aggregate. *Proc. Phys. Soc. Sect. A* **1952**, *65*, 349–354. [[CrossRef](#)]
33. Watt, J.P. Hashin-Shtrikman bounds on the effective elastic moduli of polycrystals with orthorhombic symmetry. *J. Appl. Phys.* **1979**, *50*, 6290–6295. [[CrossRef](#)]
34. Fritsch, D.; Ederer, C. Epitaxial strain effects in the spinel ferrites CoFe<sub>2</sub>O<sub>4</sub> and NiFe<sub>2</sub>O<sub>4</sub> from first principles. *Phys. Rev. B* **2010**, *82*, 104117–104127. [[CrossRef](#)]
35. Li, Z.; Fisher, E.S.; Liu, J.Z.; Nevitt, M.V. Single-crystal elastic constants of Co-Al and Co-Fe spinels. *J. Mater. Sci.* **1991**, *26*, 2621–2624. [[CrossRef](#)]
36. Idrissi, L.; Tahiri, N.; El Bounagui, O.; Ez-Zahraouy, H. Magnetic Properties of NiFe<sub>2</sub>O<sub>4</sub> Compound: Ab Initio Calculation and Monte Carlo Simulation. *J. Supercond. Novel Magn.* **2019**, *33*, 1369–1375. [[CrossRef](#)]
37. Wang, H.; Simmons, G. Elasticity of some mantle crystal structures: Pleonaste and hercynite spinel. *J. Geophys. Res.* **1972**, *77*, 4379–4392. [[CrossRef](#)]
38. Odkhuu, D.; Tsevelmaa, T.; Sangaa, D.; Tsogbadrakh, N.; Rhim, S.H.; Hong, S.C. First-principles study of magnetization reorientation and large perpendicular magnetic anisotropy in CuFe<sub>2</sub>O<sub>4</sub>/MgO heterostructures. *Phys. Rev. B* **2018**, *98*, 094408–094417. [[CrossRef](#)]
39. Yadav, R.S.; Kuřitka, I.; Vilcakova, J.; Havlica, J.; Masilko, J.; Kalina, L.; Tkacz, J.; Hajdúchová, M.; Enev, V. Structural, dielectric, electrical and magnetic properties of CuFe<sub>2</sub>O<sub>4</sub> nanoparticles synthesized by honey mediated sol–gel combustion method and annealing effect. *J. Mater. Sci. Mater. Electron.* **2017**, *28*, 6245–6261. [[CrossRef](#)]
40. Waseem, M.; Mahmood, I.; Rashid, M.; Qasim, I.; Laref, A. Investigations of physical aspects of spinel AB<sub>2</sub>O<sub>4</sub> (A = Zn, Cd) oxides via ab-initio calculations. *Phys. Lett. A* **2019**, *383*, 1810–1815. [[CrossRef](#)]
41. Dong, Y.; Lu, H.; Cui, J.; Yan, D.; Yin, F.; Li, D. Mechanical characteristics of FeAl<sub>2</sub>O<sub>4</sub> and AlFe<sub>2</sub>O<sub>4</sub> spinel phases in coatings—A study combining experimental evaluation and first-principles calculations. *Ceram. Int.* **2017**, *43*, 16094–16100. [[CrossRef](#)]
42. Moitzi, F.; Şopu, D.; Holec, D.; Perera, D.; Mousseau, N.; Eckert, J. Chemical bonding effects on the brittle-to-ductile transition in metallic glasses. *Acta Metall.* **2020**, *188*, 273–281. [[CrossRef](#)]
43. Pugh, S.F. XCII. Relations between the elastic moduli and the plastic properties of polycrystalline pure metals. *Lond. Edinb. Dublin Philos. Mag. J. Sci.* **2009**, *45*, 823–843. [[CrossRef](#)]
44. Richardson, R.C.D. The wear of metals by hard abrasives. *Wear* **1967**, *10*, 291–309. [[CrossRef](#)]
45. Nicholls, J.R.; Hall, D.J.; Tortorelli, P.F. Hardness and modulus measurements on oxide scales. *Mater. High Temp.* **2016**, *12*, 141–150. [[CrossRef](#)]
46. Ji, Z.-W.; Hu, C.-H.; Wang, D.-H.; Zhong, Y.; Yang, J.; Zhang, W.-Q.; Zhou, H.-Y. Mechanical properties and chemical bonding of the Os–B system: A first-principles study. *Acta Metall.* **2012**, *60*, 4208–4217. [[CrossRef](#)]
47. Tian, Y.J.; Xu, B.; Zhao, Z.S. Microscopic theory of hardness and design of novel super hard crystals. *Int. J. Refract. Met.* **2012**, *33*, 93–106. [[CrossRef](#)]
48. Ravindran, P.; Fast, L.; Korzhavyi, P.A.; Johansson, B.; Wills, J.; Eriksson, O. Density functional theory for calculation of elastic properties of orthorhombic crystals: Application to TiSi<sub>2</sub>. *J. Appl. Phys.* **1998**, *84*, 4891–4904. [[CrossRef](#)]
49. Ranganathan, S.I.; Ostoja-Starzewski, M. Universal elastic anisotropy index. *Phys. Rev. Lett.* **2008**, *101*, 055504. [[CrossRef](#)]
50. Luan, X.; Qin, H.; Liu, F.; Dai, Z.; Yi, Y.; Li, Q. The Mechanical Properties and Elastic Anisotropies of Cubic Ni<sub>3</sub>Al from First Principles Calculations. *Crystals* **2018**, *8*, 307. [[CrossRef](#)]
51. Wu, Q.; Li, S. Alloying element additions to Ni<sub>3</sub>Al: Site preferences and effects on elastic properties from first-principles calculations. *Comput. Mater. Sci.* **2012**, *53*, 436–443. [[CrossRef](#)]
52. Huang, B.; Duan, Y.-H.; Hu, W.-C.; Sun, Y.; Chen, S. Structural, anisotropic elastic and thermal properties of MB (M = Ti, Zr and Hf) monoborides. *Ceram. Int.* **2015**, *41*, 6831–6843. [[CrossRef](#)]
53. Wen, Y.; Wang, L.; Liu, H.; Song, L. Ab Initio Study of the Elastic and Mechanical Properties of B19TiAl. *Crystals* **2017**, *7*, 39. [[CrossRef](#)]
54. Zhu, Y.F.; Lian, J.S.; Jiang, Q. Modeling of the Melting Point, Debye Temperature, Thermal Expansion Coefficient, and the Specific Heat of Nanostructured Materials. *J. Phys. Chem. C* **2009**, *113*, 16896–16900. [[CrossRef](#)]
55. Anderson, O.L. A simplified method for calculating the Debye temperature from elastic constants. *J. Phys. Chem. Solids* **1963**, *24*, 909–917. [[CrossRef](#)]

56. Wachter, P.; Filzmoser, M.; Rebizant, J. Electronic and elastic properties of the light actinide tellurides. *Phys. B Condens. Matter* **2001**, *293*, 199–223. [[CrossRef](#)]
57. Benhalima, C.; Amari, S.; Beldi, L.; Bouhafs, B. First-Principles Study of Ferromagnetism in Iron Chromite Spinel:  $\text{FeCr}_2\text{O}_4$  and  $\text{CrFe}_2\text{O}_4$ . *Spin* **2019**, *9*, 1950014–1950026. [[CrossRef](#)]
58. Walsh, A.; Wei, S.-H.; Yan, Y.; Al-Jassim, M.M.; Turner, J.A.; Woodhouse, M.; Parkinson, B.A. Structural, magnetic, and electronic properties of the Co-Fe-Al oxide spinel system: Density-functional theory calculations. *Phys. Rev. B* **2007**, *76*, 165119–165127. [[CrossRef](#)]
59. Zhang, Y.J.; Zhang, W.; Yu, C.; Liu, Z.Y.; Yu, X.F.; Meng, F.B. Synthesis, structure and super capacitive behavior of spinel  $\text{NiFe}_2\text{O}_4$  and  $\text{NiO@NiFe}_2\text{O}_4$  nanoparticles. *Ceram. Int.* **2021**, *47*, 10063–10071. [[CrossRef](#)]
60. Clarke, D.R. Materials selection guidelines for low thermal conductivity thermal barrier coatings. *Surf. Coat. Technol.* **2003**, *163–164*, 67–74. [[CrossRef](#)]
61. Chong, X.; Jiang, Y.; Zhou, R.; Zhu, H.; Feng, J. Electronic structure, anisotropic elastic and thermal properties of the  $\eta$  phase  $\text{Fe}_6\text{W}_6\text{C}$ . *Comput. Mater. Sci.* **2015**, *108*, 205–211. [[CrossRef](#)]
62. Kim, J.; Kim, M.; Roh, K.-M.; Kang, I. Bond characteristics, mechanical properties, and high-temperature thermal conductivity of  $(\text{Hf}_{1-x}\text{Ta}_x)\text{C}$  composites. *J. Am. Ceram. Soc.* **2019**, *102*, 6298–6308. [[CrossRef](#)]
63. Ohya, Y.; Nakagawa, Z.-e.; Hamano, K. Grain-Boundary Microcracking Due to Thermal Expansion Anisotropy in Aluminum Titanate Ceramics. *J. Am. Ceram. Soc.* **1987**, *70*, C184–C186. [[CrossRef](#)]
64. Tsuru, Y.; Shimazu, M.; Shiono, M.; Morinaga, M. Evaluation of Linear Thermal Expansion Coefficients of Perovskite Oxides Using Ab-initio Molecular Dynamics with Small Cell Sizes for Materials Design. *Jpn. J. Appl. Phys.* **2010**, *49*, 045701–045706. [[CrossRef](#)]
65. Mao, X.-C.; Liu, K.; Hou, B.-S.; Tan, J.; Zhou, X.-L. Theoretical Investigation of the Structural, Elastic, and Thermodynamic Properties of  $\text{MgAl}_2\text{O}_4$  Spinel under High Pressure. *J. Phys. Soc. Jpn.* **2016**, *85*, 114605–114611. [[CrossRef](#)]
66. Suzuki, I.; Ohtani, E.; Kumazawa, M. Thermal expansion of modified spinel, beta- $\text{Mg}_2\text{SiO}_4$ . *J. Phys. Earth* **1980**, *28*, 273–280. [[CrossRef](#)]
67. Nelson, A.T.; White, J.T.; Andersson, D.A.; Aguiar, J.A.; McClellan, K.J.; Byler, D.D.; Short, M.P.; Stanek, C.R.; White, M. Thermal Expansion, Heat Capacity, and Thermal Conductivity of Nickel Ferrite ( $\text{NiFe}_2\text{O}_4$ ). *J. Am. Ceram. Soc.* **2014**, *97*, 1559–1565. [[CrossRef](#)]
68. Petric, A.; Ling, H. Electrical Conductivity and Thermal Expansion of Spinel at Elevated Temperatures. *J. Am. Ceram. Soc.* **2007**, *90*, 1515–1520. [[CrossRef](#)]